Nanoscale Horizons

ROYAL SOCIETY OF CHEMISTRY

COMMUNICATION

View Article Online
View Journal | View Issue

Cite this: *Nanoscale Horiz.*, 2025, 10, 1377

Received 9th March 2025,
Accepted 14th April 2025

DOI: 10.1039/d5nh00137d

rsc.li/nanoscale-horizons

MOF-derived nanozymes loaded with botanicals as multifunctional nanoantibiotics for synergistic treatment of intracellular antibiotic-resistant bacterial infection†

Yaling Liu,[a] Shuwen Sun,[a] Chunyao Shang,[a] Rongji Liu,[a] Chenhao Zhang,[a] Jing Yu,[a] Kai Dong, *[abc] Chen Xu*[ab] and Fangfang Cao *[d]

Intracellular bacterial infections caused by antibiotic-resistant pathogens, such as methicillin-resistant *Staphylococcus aureus* (MRSA), pose an intractable threat to public health. Intracellular MRSA is extremely difficult to eradicate using traditional antibiotics due to the poor intracellular accumulation and drug resistance. In this work, a novel multifunctional nanoantibiotic (GZNC) was constructed using MOF-derived nanozymes loaded with botanicals for synergistic treatment of intracellular antibiotic-resistant bacterial infection. The nanoantibiotic integrated glycyrrhizinic acid (GA) into ZIF-8-derived nanozymes (ZNC), which achieved controlled release of GA, excellent photothermal effects and enhanced peroxidase-like (POD-like) activity under near-infrared (NIR) light irradiation. The nanoantibiotic showed excellent potential for *in vivo* and *in vitro* eradication of intracellular antibiotic-resistant bacteria. With the merits of NIR light-actuated botanicals/photothermal therapy (PTT)/chemodynamic therapy (CDT), the nanoantibiotic could synergistically eradicate intracellular antibiotic-resistant bacteria and alleviate associated infection, providing a promising and biologically safe pathway to address the intracellular antibiotic-resistant bacterial infection.

New concepts

Intracellular MRSA infections pose an increasing threat to public health, yet there remains a lack of effective and straightforward strategies to eradicate intracellular MRSA while mitigating the growing challenge of antibiotic resistance. Here, we developed a novel near-infrared (NIR) light-responsive nanoantibiotic, composed of a MOF-derived nanozyme loaded with botanical agents, for the synergistic treatment of intracellular antibiotic-resistant bacterial infections. Upon NIR irradiation, the nanoantibiotic efficiently induced localized photothermal therapy, triggered the controlled release of GA, and enhanced its POD-like catalytic activity, leading to potent intracellular antibacterial effects. This strategy presents a promising avenue for combating intracellular bacterial infections while minimizing the risk of antibiotic resistance.

[a] *College of Chinese Medicinal Materials, Jilin Agricultural University, Changchun 130118, China. E-mail: dongkai@jlau.edu.cn, xuchen@jlau.edu.cn*
[b] *National & Local Joint Engineering Research Center for Ginseng Breeding and Development, Changchun 130118, China*
[c] *Jilin Provincial International Joint Research Center for the Development and Utilization of Authentic Medicinal Materials, Jilin Agricultural University, Changchun 130118, China*
[d] *Key Laboratory of Big Data-Based Precision Medicine of Ministry of Industry and Information Technology, School of Engineering Medicine, Beihang University, Beijing, 100191, China. E-mail: fangfangcao@buaa.edu.cn*

† Electronic supplementary information (ESI) available. See DOI: https://doi.org/10.1039/d5nh00137d

Fangfang Cao

I joined the Nanoscale Horizons Community Board in November 2023. My research centers on nanocatalytic medicine and microbial therapy. I am thrilled to contribute to this special 10th anniversary issue with our recent work on multifunctional nanozymes for antibacterial treatment, which show great promise as next-generation alternatives to traditional antibiotics. It is a real privilege to be part of this milestone. Congratulations to Nanoscale Horizons on ten outstanding years at the forefront of nanoscale science—here's to continued innovation, discovery, and impact in the years ahead!

Introduction

The emergence of bacterial drug resistance poses a serious global public health problem.[1–3] As a typical antibiotic-resistant bacterium, methicillin-resistant *Staphylococcus aureus* (MRSA) has emerged as the most obvious threat.[4–6] More seriously, MRSA can invade and survive in mammalian host cells, especially macrophages, where they can multiply and form a repository, leading to chronic and recurrent infections that induce latent infectious diseases such as osteomyelitis, sepsis and necrotizing

pneumonia.[7–9] In addition, MRSA colonization disrupts macrophage defences and provides a protective microenvironment that effectively protects bacteria against the action of antibacterial drugs and host defense mechanisms.[10] The use of high intracellular concentrations of antibiotics is essential to achieve effective treatment of infection caused by intracellular MRSA. However, antibiotics usually have problems such as low delivery efficiency, uneven intracellular distribution and short retention time, resulting in low efficacy against intracellular bacteria.[11,12] Therefore, it is necessary to design safe antibacterial agents that are not susceptible to the development of drug resistance and can effectively inhibit intracellular bacteria.[13–15]

The antibacterial potential of plant-derived natural products (PNPs) has been extensively studied. It is reported that PNPs possess remarkable antibacterial properties and have become an important source of novel antibacterial agents. More attractively, the use of PNPs as antibacterial agents is considered to be a safe and cost-effective approach to the management of bacterial infections.[16] Glycyrrhizinic acid (GA) is derived from the roots and rhizomes of *Glycyrrhiza uralensis* Fisch.[17] Of all the complexes studied to date, GA has the widest range of biological properties, such as antiviral, immune, antiallergic, antitumor and antiulcer activities,[18,19] as well as neuroprotective, hepatoprotective, and hypoglycemic effects.[20,21] In particular, GA has the structure of a phenolic compound, which is composed of glycosides and flavonoids. It is the presence of these chemical groups that gives GA excellent antibacterial activity.[22] However, GA has difficulty acting directly on intracellular bacteria. Therefore, the development of innovative delivery systems is essential to capitalize on its potential in killing intracellular antibiotic-resistant bacteria.

Nanoantibiotics are nanomaterials that have antibacterial activity or improve the efficacy and safety of antibiotics administration.[23] Ciprofloxacin and levofloxacin have been studied and encapsulated into polymer-based nanocarriers (nanoantibiotics) to improve their local bioavailability at the site of bacterial infection.[24] In order to achieve a better antibacterial effect, the concentration of nanoantibiotics needs to be increased, which may damage healthy cells.[25] In addition, several researchers have noted that for many complex bacterial infections, single-mode antibacterial technology is not effective in eradicating bacteria.[26] Combined antibacterial therapy has several advantages over single-mode antibacterial therapy, including low dosage, high efficacy, and low probability of drug resistance.[27] In recent years, MOF-derived nanozymes have been shown to possess excellent enzyme-like activities, especially peroxidase-mimicking activity, making MOF-derived nanozymes potential novel antibacterial agents.[28–31] In addition, the high specific surface area and tunable porosity of MOF-derived nanozymes facilitate the effective loading of drugs.[30,32] Under NIR light irradiation, the MOF-derived nanozymes exhibited excellent photothermal properties, which achieved the controlled release of drug and simultaneously enhanced enzyme activity.[33,34] Thus, MOF-derived nanozymes loaded with botanicals can construct a multi-modal synergistic platform for the efficient killing of intracellular antibiotic-resistant bacteria.[35] This therapeutic approach combines the benefits of single-mode therapy, reduces the dose of drug and improves the antibacterial efficacy.[36,37]

Herein, we prepared a novel NIR light-actuated nanoantibiotic based on MOF-derived nanozyme loaded with botanicals for the synergistic treatment of intracellular antibiotic-resistant bacterial infections (Scheme 1). To construct the system, MOF-derived nanozyme (ZNC) was synthesized by pyrolyzing ZIF-8 at high temperatures. The synthesized ZNC has a mesoporous structure and a high specific surface area, which enabled the efficient loading of GA. In addition, it had excellent photothermal conversion ability under NIR light, where the photothermal effect disrupted the bacterial cell membranes, resulting in the cleavage and inactivation of bacterial proteins, RNA or DNA. It also had enhanced POD-like activity.[38] ZNC with POD-like catalytic activity could induce excess H_2O_2 to catalyze the production of $^{\bullet}OH$ under the slightly acidic conditions of bacterial infection, which achieved effective antibacterial effects.[39] With the merits of NIR light-actuated botanicals/PTT/CDT, the nanoantibiotic was effective in eradicating intracellular antibiotic-resistant bacteria both *in vitro* and *in vivo* and helping to alleviate intracellular MRSA-associated subcutaneous abscess infection.

Experimental section

Materials

2-Methylimidazole, glycyrrhizic acid and gentamicin sulfate were purchased from Macklin (Shanghai, China); H_2O_2 was purchased from Aladdin (Shanghai, China); $Zn(NO_3)_2{\cdot}6H_2O$ was purchased from Xilong Science (Shantou, China); 3,3′,5,5′-tetramethylbenzidine (TMB) was purchased from Sangong (Shanghai, China); crystal violet solution was purchased from Biyuntian (Shanghai, China); agar was purchased from Solarbio (Beijing, China); MRSA (ATCC43300) was obtained from BeiJing Baocang Biotechnological Company Limited (Beijing, China); Tryptone soy broth was purchased from OXOID (UK); RAW264.7 cells (CL-0190) was purchased from Procell (Wuhan, China).

Characterization

SEM images were obtained with a HITACHI SU-8010 field emission scanning electron microscope. The particle size distributions of nanoparticles were quantified using ImageJ software. FT-IR spectroscopy spectra were obtained with a Thermo Scientific Nicolet iS20 spectrometer. UV-vis absorption spectra were recorded using a SHIMADZU UV-1900i spectrophotometer.

Preparation of GZNC

3.24 g of 2-methylimidazole was dissolved in 100 mL of methanol with stirring, denoted as A. 2.94 g of $Zn(NO_3)_2{\cdot}6H_2O$ was dissolved in 100 mL of methanol, denoted as B. Solution B was subjected to ultrasound for 15 min to form a clear solution. Solution B was subsequently added to A and then stirred vigorously for 5 h at room temperature. It was centrifuged, washed three times with methanol, and dried in a vacuum at

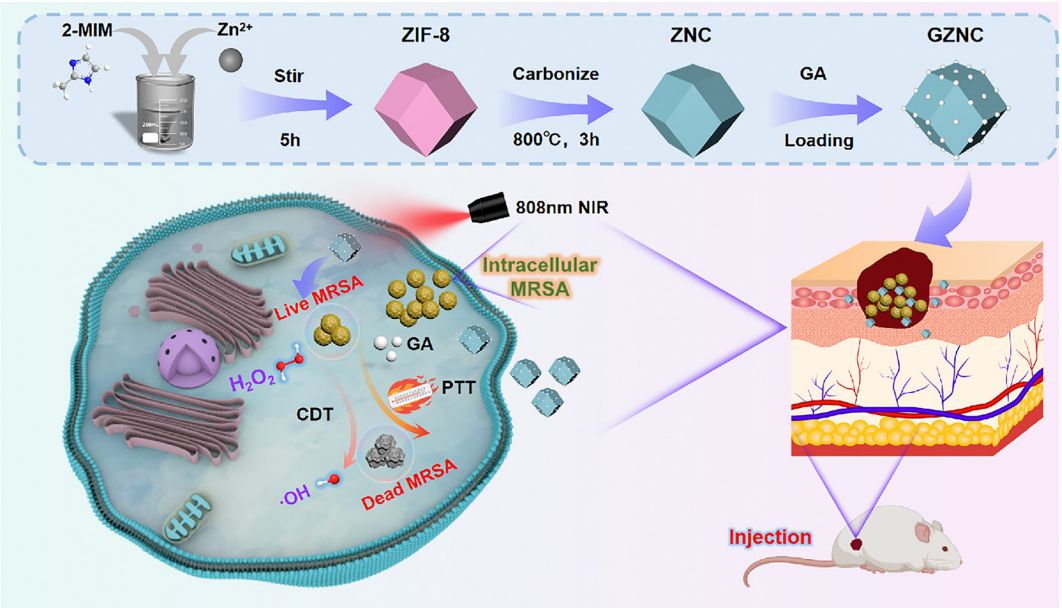

Scheme 1 NIR light-actuated botanicals/PTT/CDT for synergistic treatment of intracellular antibiotic-resistant bacterial infection.

80 °C. The powder of ZIF-8 was transferred into a porcelain boat and placed in a tube furnace. The sample was processed as follows: the temperature was increased at a rate of 5 °C min^{-1}, held at 800 °C for 3 h under flowing argon gas, and then naturally cooled to room temperature. The obtained powder was ground well in a mortar and collected for use. Next, 20 mg of ZNC was dissolved in 6 mL of deionized water, and 10 mg of GA was added. The mixture was stirred for 12 h at room temperature. After centrifugation, the sample was washed three times with deionized water to remove any adsorbed drug from the surface. GA-loaded ZNC (GZNC) was then obtained after drying.

Stability of GZNC

GZNC was stored in PBS or DMEM medium for 7 days. Subsequently, changes in the hydrodynamic diameter were assessed by DLS.

Photothermal capabilities of GZNC

The photothermal capabilities of GZNC were determined by irradiating aqueous solutions of GZNC at different concentrations (0, 50, 75, 100, and 125 μg mL^{-1}) with an 808 nm NIR laser at a power density of 1 W cm^{-2} for 10 min. The temperature was recorded every 30 s. In addition, the photothermal stability of GZNC (100 μg mL^{-1}) was assessed by five repetitive cycles of NIR laser irradiation.

Drug release properties

GZNC was added to different conditions of PBS buffer solution (pH 7.4, pH 5.5, pH 5.5 + NIR). At specific times (1, 2, 4, 6, 8, 10, 12 h), 5 mL of the soaking solution was taken to detect the released GA quantity, and an equivalent volume and pH of PBS buffer was replenished. The cumulative drug release efficiency was calculated by the release of GA at different times.

$$\text{Cumulative drug release rate } (\%) = \frac{v\sum C_{i-1} + nC_i}{m} \times 100\%$$

where v is the volume of PBS removed at each time point, C_i is the concentration of GA at the i time point, n is the total volume of the drug release system, and m is the content of GA in the GZNC.

Peroxidase-like catalytic activity

The POD-like catalytic activities of ZNC and GZNC were determined based on the colorimetric reaction of TMB oxidation in the presence of H_2O_2 in NaAc–HAc buffer solution (pH 4.0, 0.1 M). All reactions were conducted at 37 °C for 5 min, with the UV-vis absorption spectra subsequently recorded. In order to further investigate whether temperature and pH changes have an effect on catalytic activity, the same assays were performed at temperature changes from 25 °C to 75 °C and pH changes from 3.0 to 7.4. Enzymatic kinetics of ZNC were studied by measuring absorbance at 652 nm in reaction mixtures containing 1.0 mM TMB, 50 μg mL^{-1} ZNC, and H_2O_2 concentrations ranging from 0 to 25 mM, or 25 mM H_2O_2, 50 μg mL^{-1} ZNC, and TMB concentrations ranging from 0 to 1 mM. The Michaelis–Menten constant equation is as follows:

$$\frac{1}{V} = \frac{K_m}{V_{max}[S]} + \frac{1}{V_{max}}$$

where V represents the initial reaction rate, K_m denotes the Michaelis constant, [S] is the concentration of substrate, and V_{max} is the maximal reaction rate.

In vitro antibacterial experiments

A typical antibacterial experiment involved 12 groups: (1) Control; (2) Control + NIR; (3) ZNC; (4) ZNC + NIR; (5) GZNC; (6) GZNC + NIR;

(7) Control + H_2O_2; (8) Control + NIR + H_2O_2; (9) ZNC + H_2O_2; (10) ZNC + NIR + H_2O_2; (11) GZNC + H_2O_2; and (12) GZNC + NIR + H_2O_2. The NIR laser power was set at 1 W cm^{-2} for 10 min irradiation sessions. The final concentrations of H_2O_2 and bacteria were 100 μM and 1×10^4 CFU per mL, respectively. After 100 μg mL^{-1} of ZNC or GZNC were incubated with bacteria for 4 h, 100 μL of bacterial suspension was spread on agar plates. Then the agar plates were incubated at 37 °C for 12 h. The number of colonies in different treatment groups was recorded. The antibacterial rate was calculated by the following formula:

$$\text{Antibacterial rate } (\%) = \frac{N_c - N_t}{N_c} \times 100\%$$

where N_t means the number of colonies formed in the treatment group and N_c denotes the number of colonies formed in the control group.

Evaluation of the anti-biofilm activity of GZNC

In detail, 500 μL of MRSA (2×10^7 CFU per mL) was inoculated into a 24-well plate and incubated at 37 °C for 24 h. The plate was then washed with PBS buffer (pH 7.4) to obtain MRSA biofilm. After that, the above bacteria were subjected to different treatments and incubated in an incubator for 12 h. Then, after washing with PBS, 300 μL of crystal violet solution (1%) was added to a 24-cell plate and incubated in the dark for 30 min. Finally, it was washed 2 times with PBS and dried naturally at room temperature, and then 500 μL of 95% ethanol solution was added. The absorbance of different groups at 590 nm was measured to assess the biofilm biomass to reflect the anti-biofilm activity.

$$\text{Percentage of relative growth } (\%) = \frac{OD_s}{OD_c} \times 100\%$$

where OD_s and OD_c represent the absorbance of the treated and control groups respectively.

In vitro cytotoxicity

The cytotoxicity of the nanoparticles to RAW 264.7 cells was assessed by MTT assay. RAW 264.7 cells were cultured in 96-well plates at a density of 5000 cells per well. After a 24 h incubation, the fresh medium was replaced with fresh medium containing ZNC and GZNC at a concentration of 100 μg mL^{-1}. After another 24 h of incubation, 20 μL MTT was added to each well and incubated in the dark for 4 h. Then, 150 μL dimethyl sulfoxide was added to terminate the MTT reaction. Finally, the absorbance of each well was measured at 490 nm, and the cell viability was calculated as follows:

$$\text{Cell viability } (\%) = \frac{A_s - A_0}{A_c - A_0} \times 100\%$$

where A_s, A_c and A_0 represent the absorbance of the sample, control and blank groups respectively.

The cytotoxicity of samples was further assessed using live-dead staining. First, RAW 264.7 cells were cultured in a 24-well plate at a density of 1.5×10^4 cells per well and incubated for 24 h. Then, the fresh medium was replaced with ZNC and GZNC at a concentration of 100 μg mL^{-1}. After 24 h of incubation, the cells were washed with PBS. Subsequently, the cells were stained with Calcein-AM and PI for 30 min. Finally, the staining of cells was observed by fluorescence microscopy.

In vitro intracellular antibacterial assay

Firstly, the localization of GZNC in MRSA-infected RAW 264.7 cells was investigated by biological TEM imaging. Next, the intracellular antibacterial activity of GZNC was further determined by colony counting. RAW 264.7 macrophages were cultured in a 24-well plate at a density of 1×10^4 cells per well. After a 24 h incubation, the medium of each well was replaced with medium containing MRSA (1 : 20). After 1 h of infection, it was washed 3 times with PBS. Then, the medium was replaced with medium containing gentamicin (50 μg mL^{-1}) and incubated for 1 h to remove bacteria outside of macrophages. The added gentamicin and dead bacteria were removed by washing 3 times with PBS. Then different treatments were performed, and after 4 h of incubation, macrophages were lysed with PBS solution with 1% Triton-X added and serially diluted in PBS. The number of surviving bacteria in the cells was determined by plating on an agar plate.

In vivo intracellular antibacterial assay

The effect of the intracellular antibacterial *in vivo* was evaluated using a subcutaneous abscess model. ICR mice (female, 8–10 weeks, 25–30 g) were used to establish a subcutaneous abscess infected with an intracellular bacteria model. All experiments were approved by the Experimental Animal Ethics Committee of Jilin Agricultural University (ethics approval no. 2023-03-13-005). All mice were injected subcutaneously with 100 μL of MRSA suspension (10^8 CFU per mL) after anesthesia. After 24 h, the mice were injected with gentamicin (5 mg kg^{-1}) to clear the extracellular infection. After that, the mice were randomly divided into 12 groups: (1) Control; (2) Control + NIR; (3) ZNC; (4) ZNC + NIR; (5) GZNC; (6) GZNC + NIR; (7) Control + H_2O_2; (8) Control + NIR + H_2O_2; (9) ZNC + H_2O_2; (10) ZNC + NIR + H_2O_2; (11) GZNC + H_2O_2; and (12) GZNC + NIR + H_2O_2. Every 2 days, 100 μL of H_2O_2 (100 μM), ZNC (100 μg mL^{-1}), and GZNC (100 μg mL^{-1}) were injected. For the NIR irradiation group, the abscessed area was exposed to an 808 nm NIR laser (power density: 1 W cm^{-2}) for 10 min. After 10 days of treatment, the mice were euthanized, and to detect bacteria in the infected tissues, the tissues were homogenized in PBS and subsequently diluted. 100 μL of homogenate was plated onto an agar plate for colony counting. Subsequently, the tissues were fixed in 4% paraformaldehyde and hematoxylin and eosin (H&E) staining was used to observe the morphological changes in the infected tissues.

In vivo biosafety evaluation

Major organs of the mice were collected for H&E staining to assess the *in vivo* biosafety of GZNC. Next, the blood compatibility of GZNC was assessed using fresh blood samples from ICR mice. First, fresh ICR mouse blood was collected in a centrifuge tube and centrifuged to collect red blood cells

(RCBs). Then, they were washed repeatedly with saline until the supernatant was clear. The RCBs were diluted with saline and then 300 μL of RCBs were incubated with 700 μL of different concentrations of ZNC and GZNC at 37 °C for 4 h. After centrifugation at 3000 rpm for 10 min, the absorbance of the supernatant at 545 nm was recorded. The deionized water and saline treated groups were used as positive and negative control groups, respectively. The hemolysis rate was calculated as follows:

$$\text{Hemolysis } (\%) = \frac{OD_{sample} - OD_{negative}}{OD_{positive} - OD_{negative}} \times 100\%$$

where OD_{sample} is the absorbance of the groups treated with different concentrations of ZNC or GZNC, while $OD_{positive}$ and $OD_{negative}$ are the absorbance of the positive and negative control groups, respectively.

Statistical analysis

Statistical significance was determined by *t*-test and one-way ANOVA. All data were shown as mean ± SD ($n \geq 3$). GraphPad Prism software was used for inter-group comparison.

Results and discussion

Synthesis and characterization

Fig. 1A illustrates the synthesis process of GZNC. The morphology of ZIF-8 was first observed by scanning electron microscopy (SEM) and ZIF-8 exhibited a uniform and regular rhombic dodecahedral morphology (Fig. 1B). Fig. 1C shows that ZNC

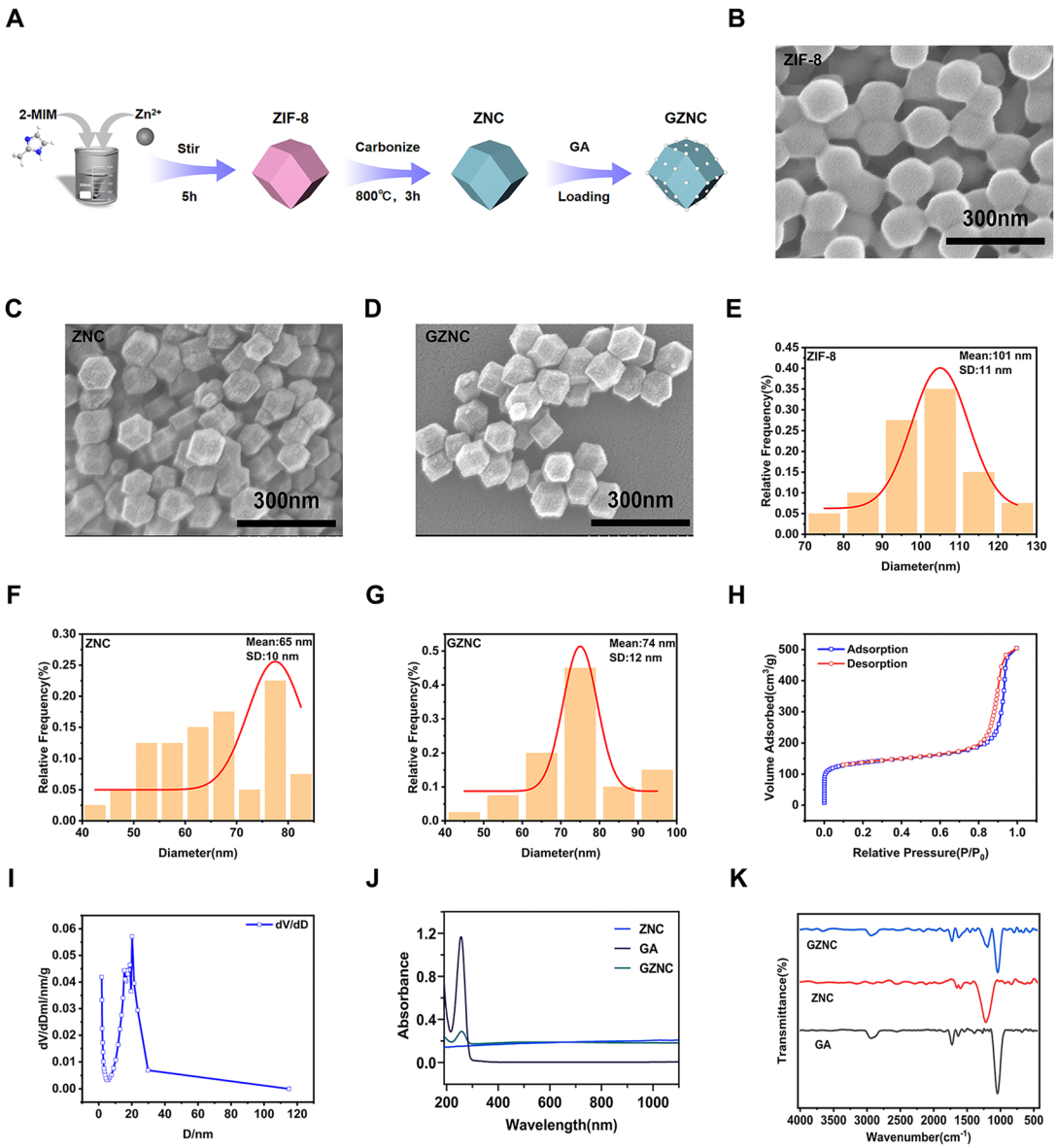

Fig. 1 Characterization of GZNC. (A) Schematic of GZNC synthesis. (B)–(D) SEM images of ZIF-8, ZNC, and GZNC. Scale bar: 300 nm. (E)–(G) Particle size distribution. (H) and (I) The N_2 adsorption–desorption isotherms of ZNC and pore size. (J) FTIR spectra. (K) UV-vis absorption spectra.

had an explicit rhombic dodecahedral shape, which agrees with that of the ZIF-8 precursor. After loading GA into ZNC, the morphology of the as-prepared GZNC was also not significantly different from that of ZNC (Fig. 1D). Fig. 1E–G show that the particle size distributions of ZIF-8, ZNC and GZNC were 101 ± 11 nm, 65 ± 10 nm and 74 ± 12 nm, respectively. The N_2 adsorption–desorption isotherm was used to determine the specific surface area as well as the pore size of ZNC, which was found to be 439.5 $m^2\ g^{-1}$ with a pore size of 12.7 nm (Fig. 1H and I) and revealed a typical mesopore of the structure and suggested that it could be used as a substrate for loading and releasing GA. The UV-vis absorption spectra of ZIF-8, ZNC and GZNC are shown in Fig. 1J. In the GZNC curve, an absorption peak at 250 nm was observed, which is the characteristic peak of GA. This indicates the successful loading of GA. The FTIR spectra of the samples are shown in Fig. 1K. The infrared spectra of GA show absorption bands at 1720 cm^{-1}, 1650 cm^{-1} and 1045 cm^{-1} corresponding to carboxyl (COOH), C═O stretching (carbonyl) and C–O stretching, respectively. Multiple characteristic peaks of GA were found in the GZNC spectrum, which further proved the successful loading of GA. Finally, we investigated the stability of GZNC. The hydrodynamic diameters of GZNC showed no significant change over one week in both PBS and DMEM media (Fig. S1, ESI†), indicating that GZNC has excellent stability.

In vitro photothermal properties

To investigate the photothermal effect of GZNC, the temperatures of GZNC solutions with different concentrations were carefully measured for 600 s. The GZNC solutions were irradiated with an 808 nm laser. As shown in Fig. 2A and B, the temperatures of GZNC solutions with different concentrations after NIR irradiation for 10 min were 39.9 °C (50 μg mL^{-1}), 43.1 °C (75 μg mL^{-1}), 45.8 °C (100 μg mL^{-1}) and 46.6 °C (125 μg mL^{-1}), respectively. As expected, the temperature of pure water (Control) increased by only 3.4 °C under the same conditions. These results indicate that GZNC had an excellent photothermal conversion capability and could efficiently convert NIR irradiation into heat. Furthermore, the temperature of GZNC (100 μg mL^{-1}) solution was recorded for 5 consecutive heating/cooling cycles. As shown in Fig. 2C, the peak temperatures of each irradiation cycle remained almost constant (46 °C, 46.4 °C, 46.5 °C, 46.4 °C, 46.1 °C), which suggested that GZNC had good stability in photothermal conversion.

Drug release properties

The drug loading rate of GA was determined using a UV-vis spectrophotometer at 250 nm. The encapsulation efficiencies and the loading efficiencies of GA in ZNC were 68.37 ± 5.52% and 34.19 ± 2.76%, respectively. Due to anaerobic fermentation of bacteria, a lot of organic acids are generated and an acidic microenvironment was created at the site of infection.[40] Thus, the pH response of the release of GA was studied. As shown in Fig. 2E, the release of GA in GZNC was assessed in neutral (pH 7.4) and acidic environments (pH 5.5) at different time intervals. The cumulative release efficiency of GA at 12 h was 37.23 ± 0.82% at pH 7.4 and 55.05 ± 3.64% at pH 5.5. This result demonstrated that the acidic microenvironment resulted in a higher release rate of GA. The enhanced release of GA from the nanoantibiotic at the site of bacterial infection would cause the superior antibacterial activity. On the other hand, the photothermal effect of GZNC could also accelerate the drug release under NIR irradiation. To determine the above description, the releasing experiment was performed at pH 5.5 with or without NIR irradiation. The release of GA was significantly increased under NIR irradiation. According to these results, it could be concluded that the drug release behaviour of GZNC was pH-dependent and could be facilitated by NIR laser, which was beneficial to combined CDT/PTT therapy.

Peroxidase-like activity

Peroxidases (POD) can exhibit the capability to catalyze the transformation of hydrogen peroxide (H_2O_2) into $^{\bullet}OH$. Therefore, we prepared a series of experiments to test the POD-like activity of ZNC by TMB assay. TMB was used as an indicator for the detection of $^{\bullet}OH$, which induced a color change from colorless to blue, accompanied by a characteristic absorption peak at 652 nm. The TMB + H_2O_2 group showed weak absorption at 652 nm while the H_2O_2 + ZNC group had no absorption. In contrast, the TMB + ZNC group showed weak absorption at 652 nm, indicating its low oxidase-like activity was negligible. The TMB + H_2O_2 + ZNC group showed the strongest absorption peak at 652 nm, indicating the strong POD-like catalytic activity of ZNC (Fig. 3B). Then, we determined the POD-like activity of different concentrations of ZNC (Fig. 3C). It was found that the POD-like activity was proportional to the concentration of ZNC. When ZNC was reacted with different concentrations of TMB and H_2O_2, the intensity of the characteristic peak at 652 nm increased with the increase of the concentration of TMB and H_2O_2 (Fig. 3D and E). This result indicated that the enzyme catalytic activity of ZNC was positively correlated with the concentrations of TMB and H_2O_2. Because infected abscess tissues usually exhibited higher acidity compared to normal tissues, the POD-like activity of ZNC was measured at different pH values to assess its catalytic performance in the infected abscess environment. As shown in Fig. 3F and G, the result indicated that the catalytic effect of ZNC was significantly stronger under weakly acidic conditions (pH 5.5) than under neutral conditions. Due to the excellent photothermal effect of ZNC, the effect of temperature on the POD-like activity of ZNC was further investigated. The POD-like activity was enhanced with increasing temperature, indicating that high temperature could increase the POD-like activity of ZNC (Fig. 3H and I). Notably, the characteristic absorption peak of ox TMB at about 652 nm was enhanced after exposure to NIR laser irradiation (Fig. 3J), which was attributed to the mild photothermal effect leading to an increase in electron transfer efficiency.[41] Moreover, the catalytic activity of drug-loaded ZNC was similar to that of unloaded at the same ZNC content, indicating that drug loading did not affect its catalytic activity (Fig. 3K).

The kinetics of the ZNC catalytic process was investigated. The Michaelis–Menten curves of ZNC were determined by changing the concentrations of TMB (Fig. 3L and M) and H_2O_2 (Fig. 3N and O). Normally, a lower K_m indicates a strong

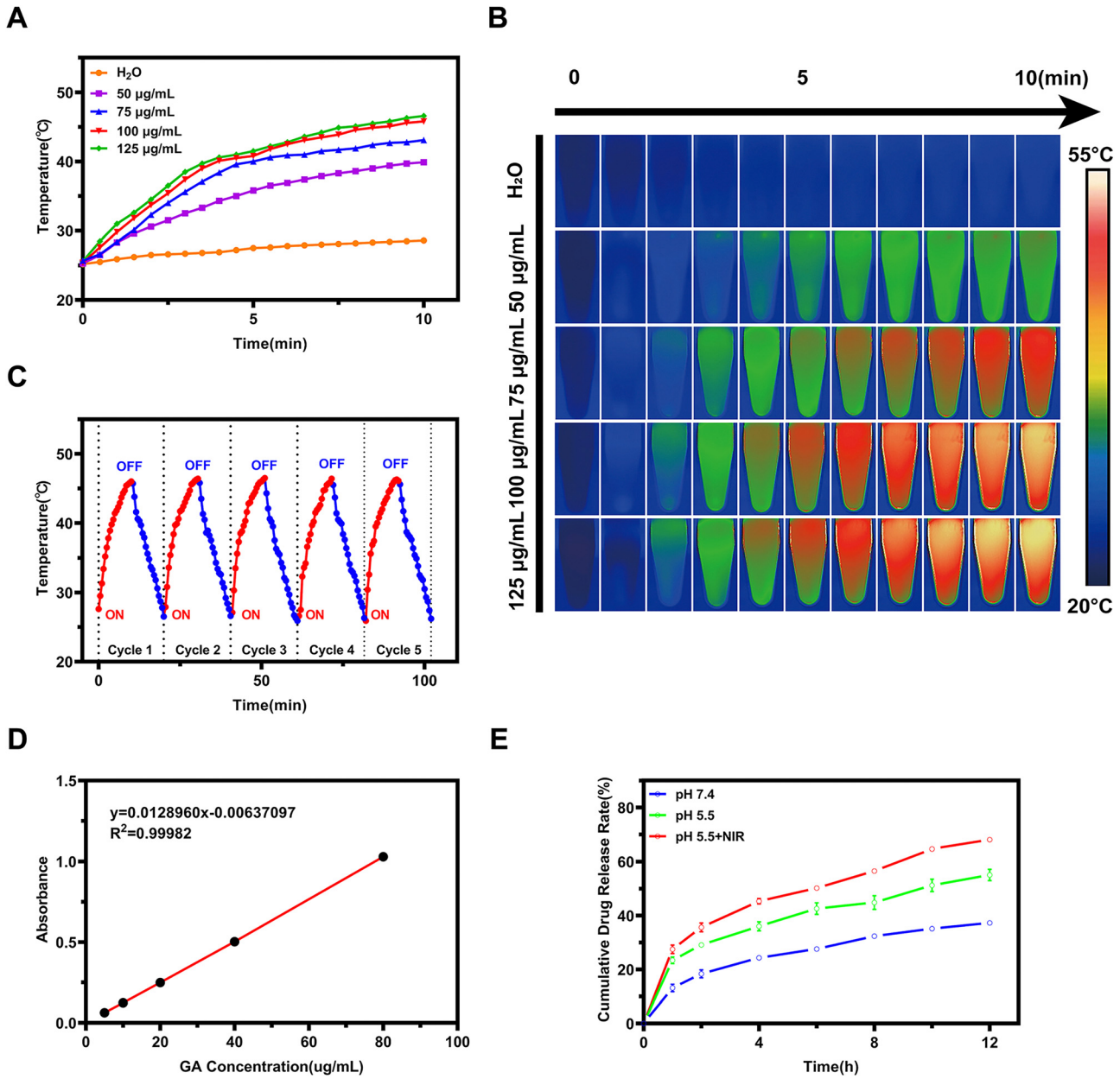

Fig. 2 Photothermal properties and drug release capacity of GZNC. (A) The temperature increase curve and (B) corresponding real-time thermography images of GZNC at different concentrations (50, 75, 100 and 125 μg mL^{-1}). (C) Photothermal stability of GZNC. (D) Standard curve of glycyrrhizinic acid. (E) Release curve of GA with different treatments.

attraction between the substrate and the catalyst, while a higher V_{max} indicates a high catalytic ability. The maximum reaction rates (V_{max} = 4.459 μM min^{-1} and 3.664 μM min^{-1}) and the Michaelis–Menten constants (K_m = 0.1057 mM and 2.115 mM) were calculated using the Lineweaver–Burk plots with TMB and H_2O_2 as the substrates. ZNC showed a smaller K_m and higher V_{max}, which suggested that it has better affinity for TMB and H_2O_2 and improved the catalytic properties to act as a peroxidase.

In vitro antibacterial activity

Considering the excellent photothermal and POD-like catalytic properties of GZNC, the potential antibacterial performance was investigated. Both *S. aureus* and MRSA were selected for the evaluation. The results showed that low concentrations of H_2O_2 (100 μM), NIR laser irradiation (1 W cm^{-2}), or their combination exhibited minimal antibacterial efficacy. In all ZNC-treated groups and the GZNC group, only a slight reduction in bacterial colonies was reduced. However, the group treated with GZNC + H_2O_2 demonstrated a significantly enhanced antibacterial effect compared to the control group, suggesting that GZNC can produce •OH by catalyzing H_2O_2. Furthermore, the GZNC + NIR group exhibited a significant reduction in bacteria, indicating that the photothermal effect of GZNC had a good antibacterial effect. Interestingly, in the GZNC + NIR + H_2O_2

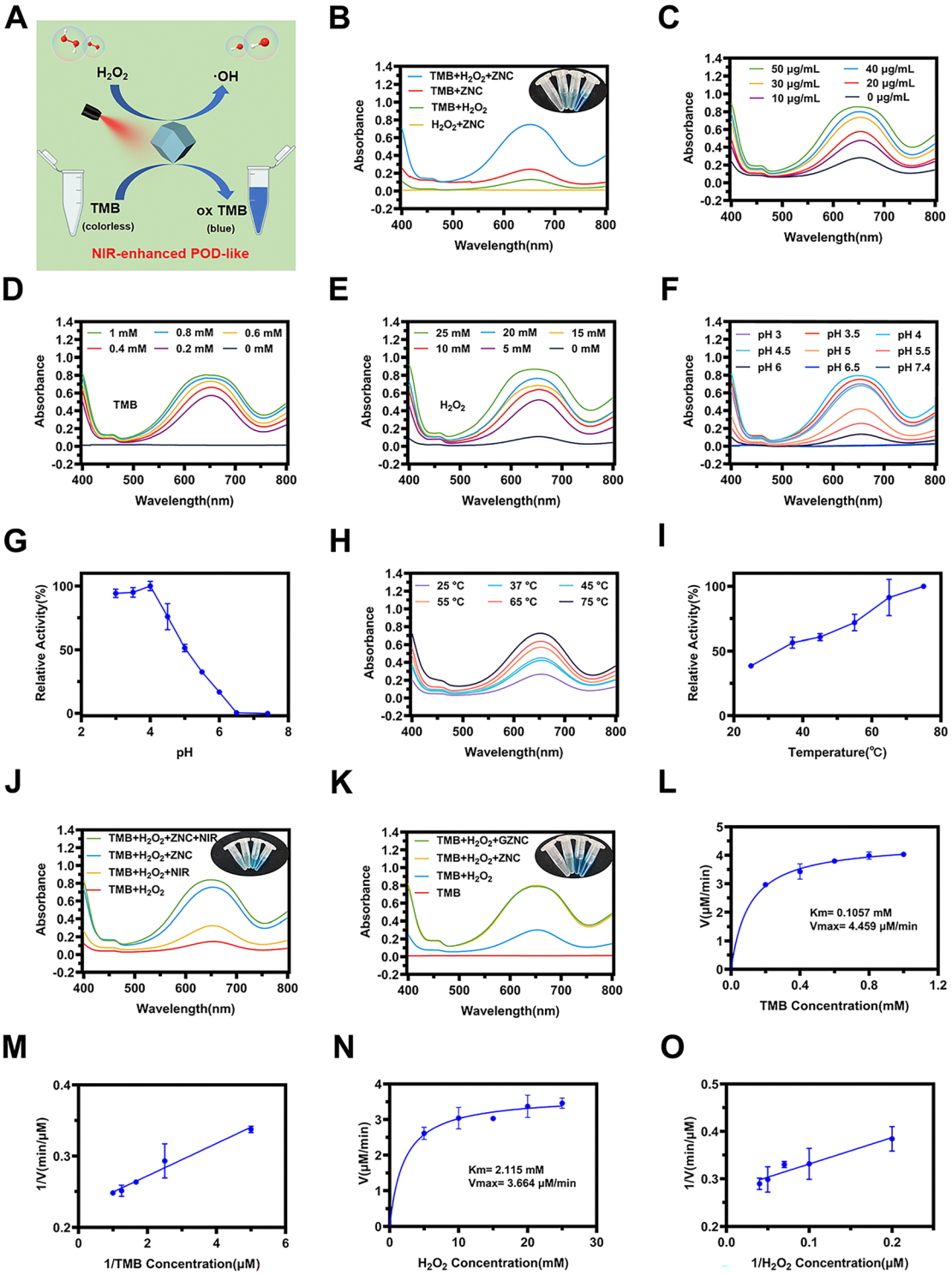

Fig. 3 The POD-like catalytic properties of ZNC. (A) Schematic of ZNC catalysis. (B) POD-like catalytic properties of ZNC in the presence of different conditions. (C–E) Catalytic performance at different concentrations of ZNC, TMB and H_2O_2. (F) and (G) The impact of pH and (H) and (I) temperature on the catalytic efficacy of ZNC. (J) and (K) Effect of NIR irradiation and drug loading on the catalytic activity of ZNC. (L) Michaelis–Menten kinetic analysis and (M) Lineweaver–Burk plotting of ZNC with TMB as the substrate. (N) Michaelis–Menten kinetic analysis and (O) Lineweaver–Burk plotting of ZNC with H_2O_2 as the substrate.

group, the bacteria were almost completely eliminated, demonstrating that the synergistic integration of the GA, CDT and PTT can successfully offset their respective shortcomings and manifest a potent antibacterial effect (Fig. 4A–D).

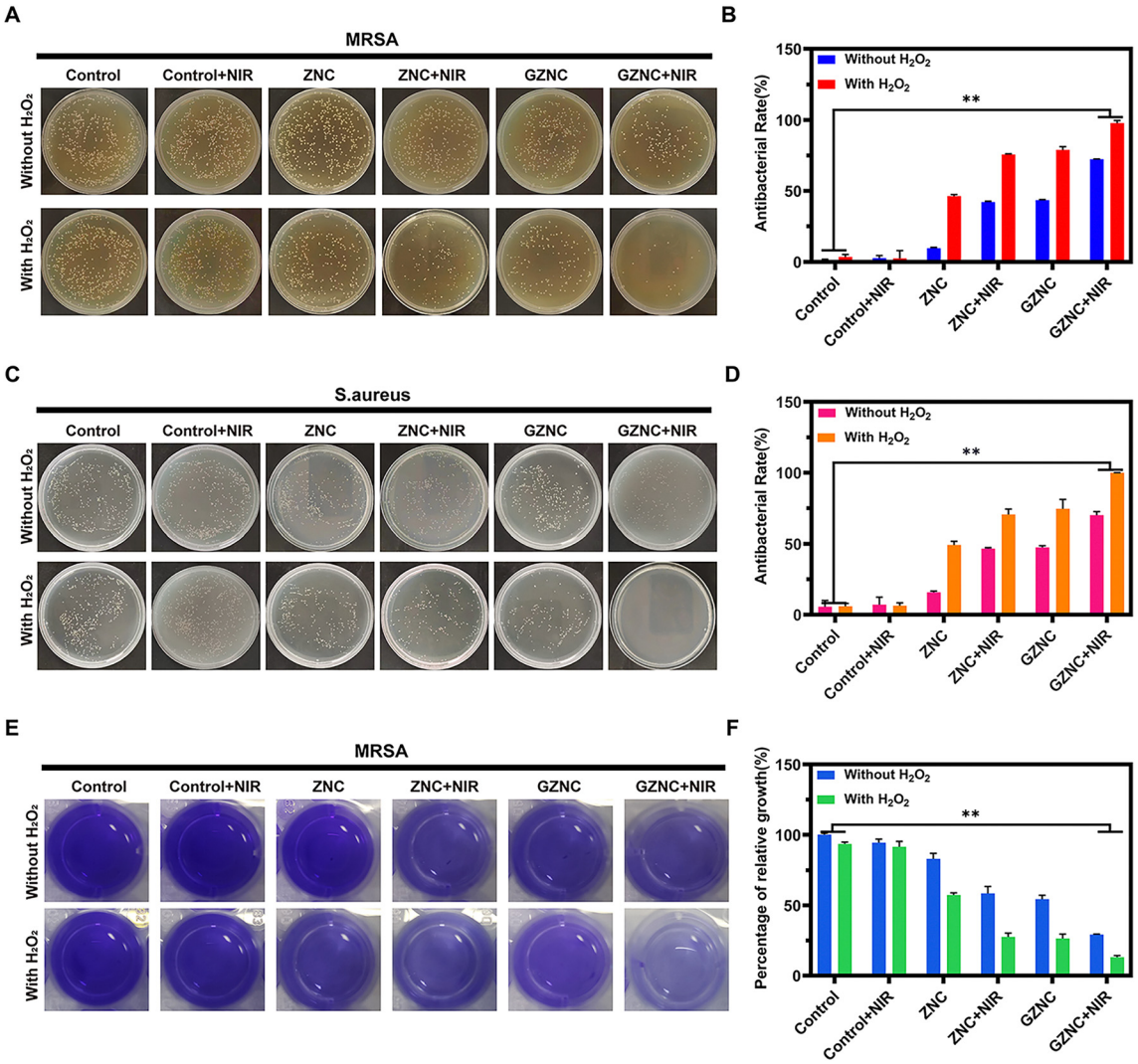

Fig. 4 *In vitro* antibacterial activity of GZNC. (A) and (B) Photographs of bacteria colonies formed by MRSA after exposure to different treatment groups and the corresponding bacterial survival rates. (C) and (D) Photographs of bacteria colonies formed by *S. aureus* after exposure to different treatment groups and the corresponding bacterial survival rates. (E) Photographs of MRSA biofilms stained with crystal violet after different treatments, and (F) relative biomass of biofilms.

Encouraged by the enhanced antibacterial properties of GZNC, anti-biofilm analysis was conducted to assess its capability to disrupt MRSA biofilms by the crystal violet staining (Fig. 4E and F). It demonstrated the significant biofilm clearance compared to the control group, when GZNC was exposed to external stimuli such as H_2O_2 or NIR. Notably, in the GZNC + H_2O_2 + NIR group, 86.90 $\pm$ 1.16% biofilm was removed. The significant antibiofilm effect was derived through the synergistic effect of GA, CDT and PTT.

In vitro biocompatibility evaluation

RAW 264.7 cells were used to assess the cytotoxicity of ZNC and GZNC. RAW 264.7 was inoculated into 96-well plates overnight as described previously. The cells were incubated with different concentrations of ZNC and GZNC for 24 h. After incubation, the viability of RAW 264.7 cells (Fig. 5A and B) were detected by MTT solution (5 mg mL^{-1}). The cell viability was greater than 85% after incubation with different concentrations of ZNC and GZNC, indicating that ZNC and GZNC had good biocompatibility. Furthermore, live/dead cells staining was performed. Fig. S2 (ESI†) showed fluorescence microscopy images of RAW 264.7 cells after co-culture with ZNC and GZNC, where a large amount of green fluorescence could be observed, while the amount of red fluorescence was negligible. This indicated that ZNC and GZNC have no obvious cytotoxicity.

In vitro intracellular antibacterial properties

To validate the intracellular antibacterial properties of GZNC, biological TEM imaging was performed to study the location of GZNC in MRSA-infected RAW 264.7 cells. An intracellular bacterial infection model was first established *in vitro*, and then GZNC was co-incubated with MRSA-infected cells. As shown in Fig. 5C, GZNC could be endocytosed by MRSA-infected macrophages and bind to invading MRSA. Furthermore, the intracellular

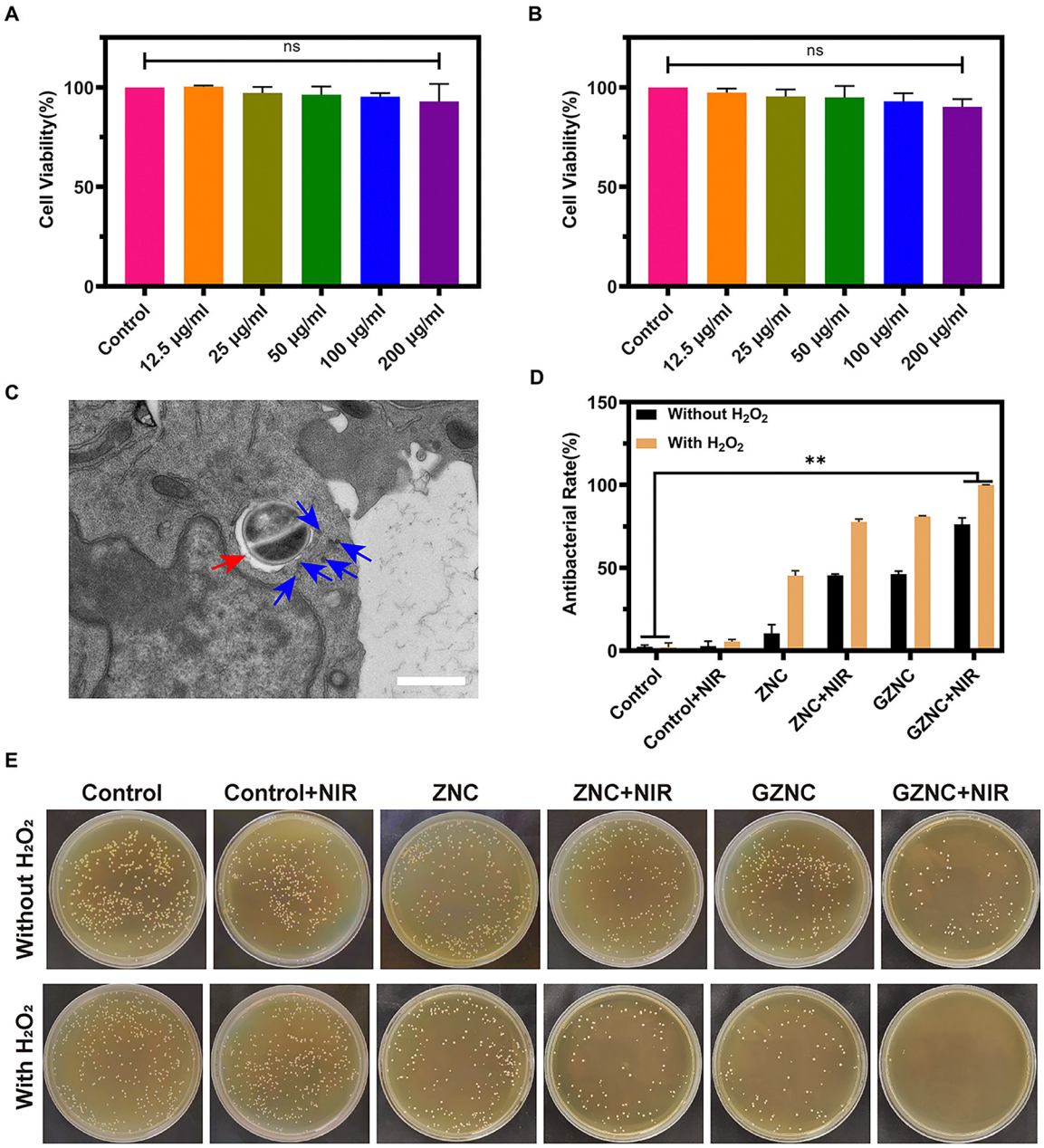

Fig. 5 Cytotoxic and intracellular antibacterial properties of GZNC. (A) and (B) Cell viability of RAW 264.7 cells with different concentrations of ZNC and GZNC treatments. (C) Bio-TEM images of MRSA-infected RAW 264.7 cells after incubation with GZNC. Red and blue arrows indicate the intracellular location of MRSA and GZNC, respectively. Scale bar: 1 μm. (D) and (E) Corresponding bacterial survival and photographs of intracellular MRSA after co-incubation with nanoparticles.

antibacterial effect of GZNC was examined in MRSA-infected RAW 264.7 cells by the plate counting method. As shown in Fig. 5D and E, GZNC had a better antibacterial effect on intracellular MRSA compared to the control group, which was attributed to GA release (46.13 ± 1.89%). In contrast, the GZNC + NIR group showed higher inhibitory ability (76.32 ± 3.85%) than the GZNC group, which was attributed to the synergistic antibacterial effects of botanicals and PTT. In addition, the GZNC + NIR + H_2O_2 group reached the highest intracellular bacterial inhibition efficacy (99.93 ± 0.11%), which was most likely attributed to the synergistic treatment of botanicals/CDT/PTT. This result emphasized the great potential of GZNC in eradicating intracellular bacteria.

In vivo intracellular antibacterial performance

We further evaluated the therapeutic effect of GZNC against intracellular bacterial infection *in vivo*. We established a subcutaneous abscess infected with an intracellular bacteria model and the experimental process is shown in Fig. 6A. The local temperature changes under 808 nm laser irradiation were recorded for PBS and GZNC *in vivo*. The temperature changes of PBS and GZNC (100 μg mL^{-1}) were monitored using an

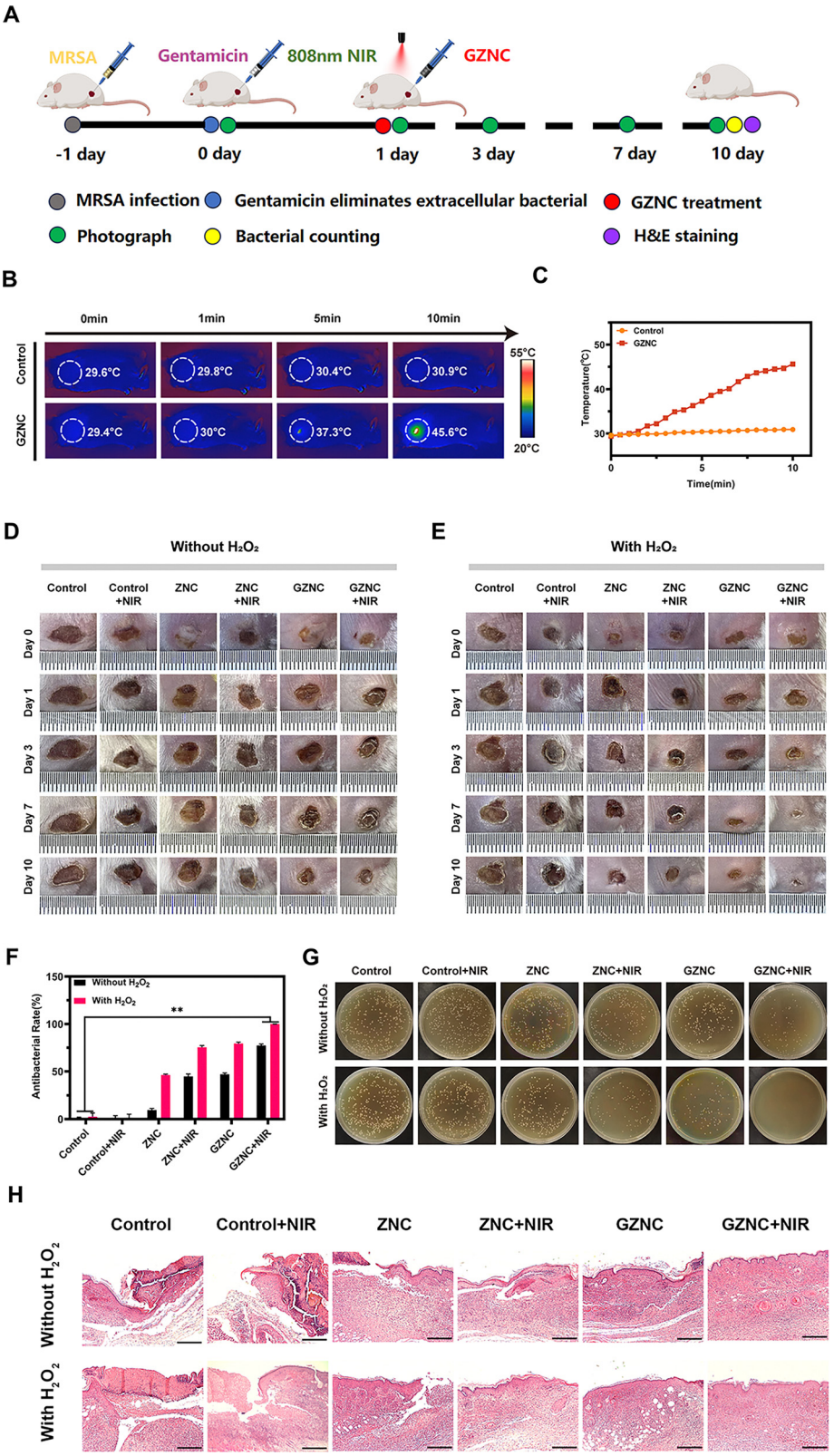

Fig. 6 Antibacterial performance *in vivo*. (A) Schematic of the GZNC antibacterial treatment regimen in an abscess model of MRSA-infected mice. (B) and (C) Thermal images and temperature profiles of skin-infected mice injected with PBS and GZNC. (D) and (E) Photographs of abscesses in mice receiving the indicated treatments for 10 days. (F) and (G) Corresponding statistical analysis of the viability of bacteria isolated from infected abscesses of mice in different treatment groups and photographs of colonies. (H) H&E staining images of skin tissues. Scale bar: 250 μm.

infrared thermal imager (Fig. 6B). After 10 min of irradiation (808 nm, 1 W cm^{-2}), the temperature of the abscess treated GZNC rapidly increased from 29.4 °C to 45.6 °C. On the other hand, the temperature of the PBS group increased slightly from 29.6 °C to 30.9 °C (Fig. 6C).

We speculate that the increase in temperature of GZNC under NIR irradiation could effectively enhance its POD-like activity, resulting in an efficient treatment against intracellular bacterial infection. As shown in Fig. 6D and E, the changes of abscesses in mice could be observed within 10 days of treatment. There was no significant recovery in the control group after 10 days. There was a slightly reduction in scar size in those treated with ZNC. The scars of mice in the GZNC group, the GZNC + NIR group and the GZNC + H_2O_2 group were smaller, and there was a significant difference compared with the control group. However, the mice treated with GZNC + NIR + H_2O_2 showed the fastest recovery and the scars almost completely disappeared, which was attributed to the synergistic antibacterial effects of CDT, PTT and GA. The bacterial suspension extracted from the abscess site was subjected to colony counting to evaluate the bactericidal effect of different treatment groups. As shown in Fig. 6F and G, the intracellular antibacterial performance *in vivo* was comparable to the results *in vitro*, with the GZNC + NIR + H_2O_2 group showing the most potent antibacterial effect, with markedly fewer bacterial colonies than other groups.

The healing of infected skin tissue was further evaluated with H&E staining (Fig. 6H). In the control group, a large amount of inflammatory cell infiltration and diffuse swelling were observed at the site of infection. In addition, the infected tissue was separated from the pus cavity, and the wound was covered by thick crusts. At the same time, all ZNC-treated groups showed relatively reduced inflammation. In contrast, a small amount of inflammatory cell infiltration with incomplete epidermal regeneration was observed in the GZNC group, GZNC + NIR group and the GZNC + H_2O_2 group. This was due to the limitations of relying solely on the drug, CDT, or PTT for intracellular antibiotic-resistant bacterial elimination. However, new hair follicles and complete epithelial tissue formation were observed in the GZNC + NIR + H_2O_2 group. Therefore, GZNC can effectively treat intracellular MRSA-infected subcutaneous abscesses through multi-modal synergistic antibacterial effects, providing a novel strategy for clinical treatment of intracellular antibiotic-resistant bacterial infections.

In vivo biocompatibility evaluation

To evaluate the biocompatibility of ZNC and GZNC *in vivo*, we investigated their effects on erythrocytes. As shown in Fig. S3A and B (ESI†), the supernatants treated with saline and different concentrations of ZNC and GZNC solutions were clear and colourless, and the supernatants treated with deionized water were bright red. As shown in the Fig. S3A and B (ESI†), the hemolysis rate of GZNC is 0.09% and was well below the permissible limit (5%). The results indicated that these materials have negligible hemolytic effect on erythrocytes. In addition, we performed H&E staining on the major organs of the heart, liver, spleen, lungs and kidneys of mice in each experimental group, as shown in Fig. S4A and B (ESI†). Compared with healthy mice, the H&E-stained sections of the major organs from each treatment group showed no signs of inflammation or substantial damage, indicating that these materials exhibited no adverse effects and possessed good biosafety. The results indicated that our deigned synergistic antibacterial platform is both safe and effective, highlighting its promising potential for clinical application.

Conclusions

In summary, we prepared a NIR light-actuated nanoantibiotic for multi-modal synergistic therapy with botanicals/PTT/CDT against intracellular antibiotic-resistant bacterial infection. Under NIR light irradiation, the nanoantibiotic was able to effectively perform localized photothermal therapy, controlled the release of GA and enhanced POD-like catalytic activity for effective intracellular antibacterial effects. *In vitro* experiments showed that this synergistic antibacterial strategy was effective against intracellular MRSA. In addition, the nanoantibiotic showed significant results in the treatment of intracellular MRSA-associated subcutaneous abscess infections. This strategy provides a potential alternative to enhancing intracellular antibiotic-resistant bacterial therapy, especially for repetitive and long-term clinical applications.

Author contributions

Yaling Liu: conceptualization, methodology, investigation, formal analysis, visualization, writing – original draft. Shuwen Sun: investigation, formal analysis, visualization. Chunyao Shang: investigation, formal analysis, visualization. Rongji Liu: methodology, investigation, formal analysis. Chenhao Zhang: investigation, formal analysis, visualization. Jing Yu: investigation, formal analysis, visualization. Kai Dong: resources, writing – review & editing, supervision, project administration, funding acquisition. Chen Xu: resources, writing – review & editing, supervision, project administration, funding acquisition. Fangfang Cao: resources, writing – review & editing, supervision, project administration.

Data availability

The authors declare that the data supporting the findings of this study are available within the paper and the ESI.†

Conflicts of interest

There are no conflicts to declare.

Acknowledgements

This work was supported by the Jilin Scientific and Technological Development Program (20240101033JJ), the National

Natural Science Foundation of China (22477042) and the Scientific research start-up funds of Jilin Agricultural University (2021003).

References

1 J. Han, S. Zeng, Y. Chen, H. Li and J. Yoon, *Adv. Drug Delivery Rev.*, 2023, **193**, 114672.
2 F. Li, K. Huang, H. Chang, Y. Liang, J. Zhao, S. Yang and F. Liu, *Acta Biomater.*, 2022, **150**, 380–390.
3 X. Chu, P. Zhang, Y. Wang, B. Sun, Y. Liu, Q. Zhang, W. Feng, Z. Li, K. Li, N. Zhou and J. Shen, *Carbon*, 2021, **176**, 126–138.
4 X. Zou, S. Cai, T. Wang, S. Zheng, X. Cui, J. Hao, X. Chen, Y. Liu, Z. Zhang and Y. Li, *Acta Biomater.*, 2023, **169**, 410–421.
5 J. J. Aguilera-Correa, M. Gisbert-Garzarán, A. Mediero, M. J. Fernández-Aceñero, D. de-Pablo-Velasco, D. Lozano, J. Esteban and M. Vallet-Regí, *Acta Biomater.*, 2022, **154**, 608–625.
6 J. Trousil, N.-J. K. Dal, F. Fenaroli, I. Schlachet, P. Kubíčková, O. Janoušková, E. Pavlova, M. Škorič, K. Trejbalová, O. Pavliš and A. Sosnik, *Small*, 2022, **18**, 2201853.
7 H. Liu, X. Liu, H. Wang, J. Ren and X. Qu, *Small*, 2023, **19**, 2207510.
8 M. G. Elnaggar, K. Jiang, H. E. Eldesouky, Y. Pei, J. Park, S. A. Yuk, F. Meng, A. M. Dieterly, H. T. Mohammad, Y. A. Hegazy, H. M. Tawfeek, A. A. Abdel-Rahman, A. E. Aboutaleb, M. N. Seleem and Y. Yeo, *Biomaterials*, 2020, **262**, 120344.
9 D. Zhao, W. Feng, X. Kang, H. Li, F. Liu, W. Zheng, G. Li and X. Wang, *J. Mater. Chem. B*, 2023, **11**, 2958–2971.
10 Z. Tang, S. Liu, N. Chen, M. Luo, J. Wu and Y. Zheng, *Colloids Surf., B*, 2021, **205**, 111899.
11 B. Xie, H. Zhao, R. Zhang, Y. Ding, C. Gao, Y. He and R. Wang, *J. Controlled Release*, 2023, **357**, 371–378.
12 W. Feng, M. Chittò, T. F. Moriarty, G. Li and X. Wang, *Macromol. Biosci.*, 2023, **23**, 2200311.
13 Q. Tang, P. Tan, Z. Dai, T. Wang, S. Xu, Y. Ding, J. Jin, X. Zhang, Y. Zhang, C. Zhou, Z. Yue, H. Fu, J. Yan and X. Ma, *Acta Biomater.*, 2023, **157**, 210–224.
14 Q. Xiao, B. Mai, Y. Nie, C. Yuan, M. Xiang, Z. Shi, J. Wu, W. Leung, C. Xu, S. Q. Yao, P. Wang and L. Gao, *ACS Appl. Mater. Interfaces*, 2021, **13**, 11588–11596.
15 Y. Liao, B. Li, H. Chen, Y. Ma, F. Wang, L. Huang, B. Shen, H. Song and P. Yue, *J. Controlled Release*, 2025, **378**, 60–91.
16 F. J. Álvarez-Martínez, R. Díaz-Puertas, E. Barrajón-Catalán and V. Micol, in *Natural Products as Sources of Novel Drugs*, ed. C. L. Wainwright and V. B. Schini-Kerth, Springer Nature, Switzerland, Cham, 2025, pp. 265–293, DOI: 10.1007/164_2024_706.
17 Z. Xu, Z. Gao, J. Lu, T. Wang, W. Wang, L. Fan, J. Xi and B. Han, *Colloids Surf., B*, 2023, **221**, 112977.
18 G. El-Saber Batiha, A. Magdy Beshbishy, A. El-Mleeh, M. M. Abdel-Daim and H. Prasad Devkota, *Biomolecules*, 2020, **10**, 352.
19 Y. Wen, H. Chen, L. Zhang, M. Wu, F. Zhang, D. Yang, J. Shen and J. Chen, *Free Radicals Biol. Med.*, 2021, **173**, 41–51.
20 W. Zhang, T. Li, X.-J. Zhang and Z.-Y. Zhu, *Food Funct.*, 2020, **11**, 4160–4170.
21 E. Olchowik-Grabarek, K. Czerkas, A. D. Matchanov, R. S. Esanov, U. D. Matchanov, M. Zamaraeva and S. Sekowski, *J. Funct. Biomater.*, 2023, **14**, 368.
22 J. C. Lee, L. H. Seksama, C. H. Park and C. S. Kim, *Mater. Lett.*, 2023, **338**, 134030.
23 J. A. Edson and Y. J. Kwon, *Nano Convergence*, 2016, **3**, 26.
24 H. Le, E. Dé, D. Le Cerf and C. Karakasyan, *Antibiotics*, 2023, **12**, 1066.
25 X. Li, W. Du, W. Xu, G. Ling and P. Zhang, *J. Mater. Chem. B*, 2023, **11**, 4354–4364.
26 T. Du, B. Huang, J. Cao, C. Li, J. Jiao, Z. Xiao, L. Wei, J. Ma, X. Du and S. Wang, *ACS Omega*, 2022, **7**, 18339–18349.
27 M. J. Hakeem, J. Feng, L. Ma, L. Ma and X. Lu, *Microbiol. Res.*, 2023, **266**, 127246.
28 C. Zhou, Q. Wang, J. Jiang and L. Gao, *Antibiotics*, 2022, **11**, 390.
29 P. Wu, F. Gong, X. Feng, Y. Xia, L. Xia, T. Kai and P. Ding, *J. Nanobiotechnol.*, 2023, **21**, 185.
30 J. Liu, D. Wu, N. Zhu, Y. Wu and G. Li, *Trends Food Sci. Technol.*, 2021, **109**, 413–434.
31 M. Shen, F. Forghani, X. Kong, D. Liu, X. Ye, S. Chen and T. Ding, *Compr. Rev. Food Sci. Food Saf.*, 2020, **19**, 1397–1419.
32 L. Guo, Y. Chen, T. Wang, Y. Yuan, Y. Yang, X. Luo, S. Hu, J. Ding and W. Zhou, *J. Controlled Release*, 2021, **330**, 119–131.
33 X. Zhu, W. Zhang, H. Xiang, Q. Chang, R. Liu, Y. Wan, R. Zhang, F. Zhao, Y. She, H. Yuan, J. Yang, Q. Li, S. Wang and L. Yan, *Nano Today*, 2023, **50**, 101836.
34 Q. Wang, J. Jiang and L. Gao, *WIREs Nanomed. Nanobiotechnol.*, 2022, **14**, e1769.
35 K. Dong, W. Lin, T. Zhu, S. Sun, C. Zhang, C. Xu, F. Cao and X. Chen, *Adv. Healthcare Mater.*, 2024, 2401657.
36 Z. Liu, X. Zhao, B. Yu, N. Zhao, C. Zhang and F.-J. Xu, *ACS Nano*, 2021, **15**, 7482–7490.
37 Y. Sang, W. Li, H. Liu, L. Zhang, H. Wang, Z. Liu, J. Ren and X. Qu, *Adv. Funct. Mater.*, 2021, **31**, 2110449.
38 J. Guo, W. Wei, Y. Zhao and H. Dai, *Regener. Biomater.*, 2022, **9**, rbac041.
39 Y. Li, W. Ma, J. Sun, M. Lin, Y. Niu, X. Yang and Y. Xu, *Carbon*, 2020, **159**, 149–160.
40 S. Gui, X. Li, M. Feng, H. Liu, L. Huang and X. Niu, *Front. Bioeng. Biotechnol.*, 2023, 11.
41 Y. Liu, B. Xu, M. Lu, S. Li, J. Guo, F. Chen, X. Xiong, Z. Yin, H. Liu and D. Zhou, *Bioact. Mater.*, 2022, **12**, 246–256.